

# Deep Eastern Boundary Currents: Idealized Models and Dynamics

XIAOTING YANG,<sup>a</sup> ELI TZIPERMAN,<sup>a,b</sup> AND KEVIN SPEER<sup>c,d</sup>

<sup>a</sup> *Department of Earth and Planetary Sciences, Harvard University, Cambridge, Massachusetts*

<sup>b</sup> *School of Engineering and Applied Sciences, Harvard University, Cambridge, Massachusetts*

<sup>c</sup> *Geophysical Fluid Dynamics Institute, Florida State University, Tallahassee, Florida*

<sup>d</sup> *Department of Scientific Computing, Florida State University, Tallahassee, Florida*

(Manuscript received 17 September 2020, in final form 28 December 2020)

**ABSTRACT:** Concentrated poleward flows along eastern boundaries between 2- and 4-km depth in the southeast Pacific, Atlantic, and Indian Oceans have been observed, and appear in data assimilation products and regional model simulations at sufficiently high horizontal resolution, but their dynamics are still not well understood. We study the local dynamics of these deep eastern boundary currents (DEBCs) using idealized GCM simulations, and we use a conceptual vorticity model for the DEBCs to gain additional insights into the dynamics. Over most of the zonal width of the DEBCs, the vorticity balance is between meridional advection of planetary vorticity and vortex stretching, which is an interior-like vorticity balance. Over a thinner layer very close to the eastern boundary, a balance between vorticity tendencies due to friction and stretching that rapidly decay away from the boundary is found. Over the part of the DEBC that is governed by an interior-like vorticity balance, vertical stretching is driven by both the topography and temperature diffusion, while in the thinner boundary layer, it is driven instead by parameterized horizontal temperature mixing. The topographic driving acts via a cross-isobath flow that leads to stretching and thus to vorticity forcing for the concentrated DEBCs.

**KEYWORDS:** Boundary currents; Ocean circulation; Potential vorticity; Ocean models

## 1. Introduction

In a companion of this study (Yang et al. 2020a), deep eastern boundary currents (DEBCs) present in the Southern Ocean State Estimate (SOSE; Mazloff et al. 2010) and in realistic high-resolution regional simulations using the MITgcm (Marshall et al. 1997) were analyzed. The results showed persistent flows in the Atlantic, Pacific, and Indian Oceans in the Southern Hemisphere, with significant signatures in tracer and potential vorticity distributions and mass transports, consistent with the somewhat sparse observations reviewed by Yang et al. (2020a). The vorticity budget of the DEBCs showed that they are driven by an interior-like balance between vortex stretching and the beta effect, except very near the eastern boundary, where a clear signature of a different balance is seen. This near-boundary balance is between horizontal temperature diffusion (parameterized mixing) and horizontal friction, as discussed in the context of linear circulation in a rotating stratified fluid (Barcilon and Pedlosky 1967; LaCasce 2004; Gjermundsen and LaCasce 2017; Bire and Wolfe 2018; Wolfe and Bire 2019; Bire 2019). In this paper we provide a comprehensive analysis of the dynamics of these currents both using idealized regional GCM configurations motivated by the geometry and bathymetry of the three basins, and using a highly simplified linearized vorticity model introduced in Yang et al. (2020b).

Near-surface and subsurface shallow eastern boundary currents (SEBCs) are commonly observed in eastern boundary regions (e.g., Hickey 1979; Thompson 1984; Peliz et al. 2003) and have received a great deal of attention. It is important to determine, therefore, if the dynamics of these SEBCs are relevant to their deep counterparts that are the subject of this paper. The driving of the SEBCs may involve isopycnal tilting due to surface wind forcing (Choboter et al. 2005) or a meridional surface buoyancy gradient (McCreary et al. 1986; Bire and Wolfe 2018). The cross-shore variation of the nearshore wind plays an important role in determining the width and strength of the SEBCs (Capet et al. 2004). The existence of such currents is usually explained by some trapping mechanism near the eastern boundary. The structure of these upper ocean eastern boundary currents and undercurrents is found to be sensitive to the topography (McCreary and Chao 1985), because topography alters the propagation characteristics of Rossby waves by vortex stretching, trapping flow on the eastern boundary by restraining westward propagation (Furue et al. 2013). Benthuisen et al. (2014) showed that an eastern intensified current can arise from the interaction between the surface layer and the bottom topography, with small diapycnal mixing and without resolved eddies. The width and the transport of the upper ocean currents are sensitive to the upwelling that drives these currents (McCreary 1981; McCreary and Chao 1985; McCreary et al. 1986, 1987; Benthuisen et al. 2014). SEBCs can also be generated by a strong eastward zonal flow forced by surface wind that nonlinearly traps an eastern boundary current (McCreary et al. 1992).

Time dependence is also an important dynamical factor for the SEBCs. For example, Rossby waves excited along the eastern boundary by fast trapped coastal waves can maintain a

Supplemental information related to this paper is available at the Journals Online website: <https://doi.org/10.1175/JPO-D-20-0227.s1>.

Corresponding author: Xiaoting Yang, [xiaoting\\_yang@g.harvard.edu](mailto:xiaoting_yang@g.harvard.edu)

DOI: 10.1175/JPO-D-20-0227.1

© 2021 American Meteorological Society. For information regarding reuse of this content and general copyright information, consult the [AMS Copyright Policy](#) ([www.ametsoc.org/PUBSReuseLicenses](http://www.ametsoc.org/PUBSReuseLicenses)).

cross-shore pressure gradient that drives an eastern boundary current (Samelson 2017). Similarly, Bire and Wolfe (2018) found that momentum transport due to time-dependent eddies and to form drag is important for eastern boundary currents forced by a surface meridional buoyancy gradient, while lateral friction is only important very close to the eastern boundary. The zonal scale of the current in this case is set by the zonal structure of the form drag, which is strong at the seaward side of the current, but weaker closer to the eastern boundary. This will be relevant to our findings regarding DEBCs below. While this rich literature on the steady state and time-dependent SEBCs is potentially very relevant to the dynamics of DEBCs, we show below that a different mechanism supports flows in DEBCs near the eastern boundary.

Some discussion of deep currents near the eastern boundary can be found in papers concerning different aspects of the deep ocean circulation. In a study of the deep Mediterranean outflow, Tziperman (1987) suggested that eastward intensified solutions can be trapped by vertical diffusion which damps waves propagating westward from the boundary. Accordingly, eastern boundary currents can arise when the vertical diffusion is sufficiently large (McCreary et al. 1986; Kawase 1987; Weaver and Middleton 1989; Park 2006). In a layered model of the Antarctic Bottom Water forced by uniform upwelling, Stephens and Marshall (2000) found an enhanced flow near the eastern boundary, yet did not discuss its mechanism. Nof and Olson (1993) suggested that a current crossing the equator northward in a trench would tend to move from the western side to the eastern side of the trench. The interior south-eastward pathway of deep water in the South Atlantic Ocean which feeds the southward deep eastern boundary current in the Cape Basin (Hogg and Thurnherr 2005) has been explained by eddy thickness transport due to energetic Agulhas rings (van Sebille et al. 2012) as discussed in Yang et al. (2020a). The generation of mean bottom flows via the interaction of ocean eddies and rough bottom topography, was also analyzed via the tools of statistical physics by Holloway (1992).

In this work we design idealized GCM experiments to identify the essential local DEBC dynamics, by eliminating surface forcing and idealizing the geometry and bathymetry. Based on the idealized GCM results, we proceed to develop a simple linear vorticity model that can reproduce the most important features of the vorticity dynamics of both the realistic GCM simulations in Yang et al. (2020a) and the idealized GCM simulations analyzed here. The resulting hierarchy of models, from SOSE and the realistic simulations of Yang et al. (2020a), to the idealized GCM and even simpler vorticity equation used here, enable us to decompose the DEBC dynamics into its key elements. This paper is organized as follows: section 2 presents the results and vorticity budgets of the idealized GCM experiments. In section 3 we derive the simple vorticity model, analyze the eigenmodes of the vorticity model, identify decaying modes from the eastern and western boundaries over a very broad parameter regime, and use the results to discuss the dynamics of the GCM solutions. Then, a vertically integrated version of the vorticity model is used to

study the role of topography and stratification. We conclude in section 4.

## 2. Idealized simulations of DEBCs using a GCM

In this section we first present the GCM setups used for the different model experiments (section 2a), and then the GCM results (section 2b), followed by an analysis of the vorticity budget (section 2c).

### a. The GCM setup

We use idealized configurations of the Massachusetts Institute of Technology General Circulation Model (MITgcm; Marshall et al. 1997) motivated by the geometry and topography of the southeast Pacific/Atlantic/Indian Oceans (Figs. 1a–c), to study the dynamics of deep eastern boundary currents. For the southeast Pacific Ocean, the bathymetry is an idealized trench constructed from a polynomial fit to the realistic Peru–Chile Trench at 30°S, and a flat bottom to the west of the trench. In the southeast Atlantic Ocean, the bathymetry is a gentle slope, again based on a polynomial fit to the realistic continental slope in the southeast Atlantic Ocean at 30°S. For the southeast Indian Ocean, a seamount which has a Gaussian profile in both the zonal and meridional directions is added not far from the eastern boundary, idealizing the Naturaliste Plateau of the Indian Ocean that was suggested to support deep eastern boundary flows on its western flank (Toole and Warren 1993; Sloyan and Rintoul 2001). The maximum height of the seamount is 3 km, and its center is at 32°S and 113°E. In addition, an idealized slope is prescribed from a polynomial fit to the realistic bathymetry in the southeast Indian Ocean.

The horizontal resolution for the idealized configuration is 0.1° in the zonal direction and  $0.1^\circ \times \cos(\theta)$  in the meridional direction ( $\theta$  is latitude), leading to near-square cells. There are 64 vertical layers whose thicknesses range from 10 m near the surface to 125 m near the bottom. The sizes of the domains of each experiment are 14.4° wide and from 49.8° to 26°S (idealized Pacific), 18° wide and from 38.1° to 24.9°S (Atlantic), and 12° wide and from 35.7° to 24.9°S (Indian). The domain sizes of the idealized Pacific and Atlantic configurations are the same as their “realistic” counterparts in Yang et al. (2020a). The idealized Indian configuration domain is narrower to allow us to focus on the role of the seamount instead of the southward outflow south of Australia emphasized in Yang et al. (2020a).

There are open boundaries in the north, south and west of each regional domain. The stratification is restored in sponge layers near these boundaries to the zonal average of SOSE on the northern boundary of each ocean domain. Inflow/outflow boundary conditions are imposed in the northern and southern boundary sponge layers (Figs. 1a–c) to drive a deep DEBC whose local dynamics are the focus of this paper; the inflow and outflow have a Gaussian shape peaking at 2.5-km depth, decaying in the zonal direction with a scale of 200 km, and in the vertical direction with a scale of 500 m, with specified corresponding boundary isotherms tilting relative to the reference stratification according to thermal wind balance. The restoring time scale in the 20-grid-point thick sponge layers is one day on the outer edge, transitioning linearly in space to 20 days on the

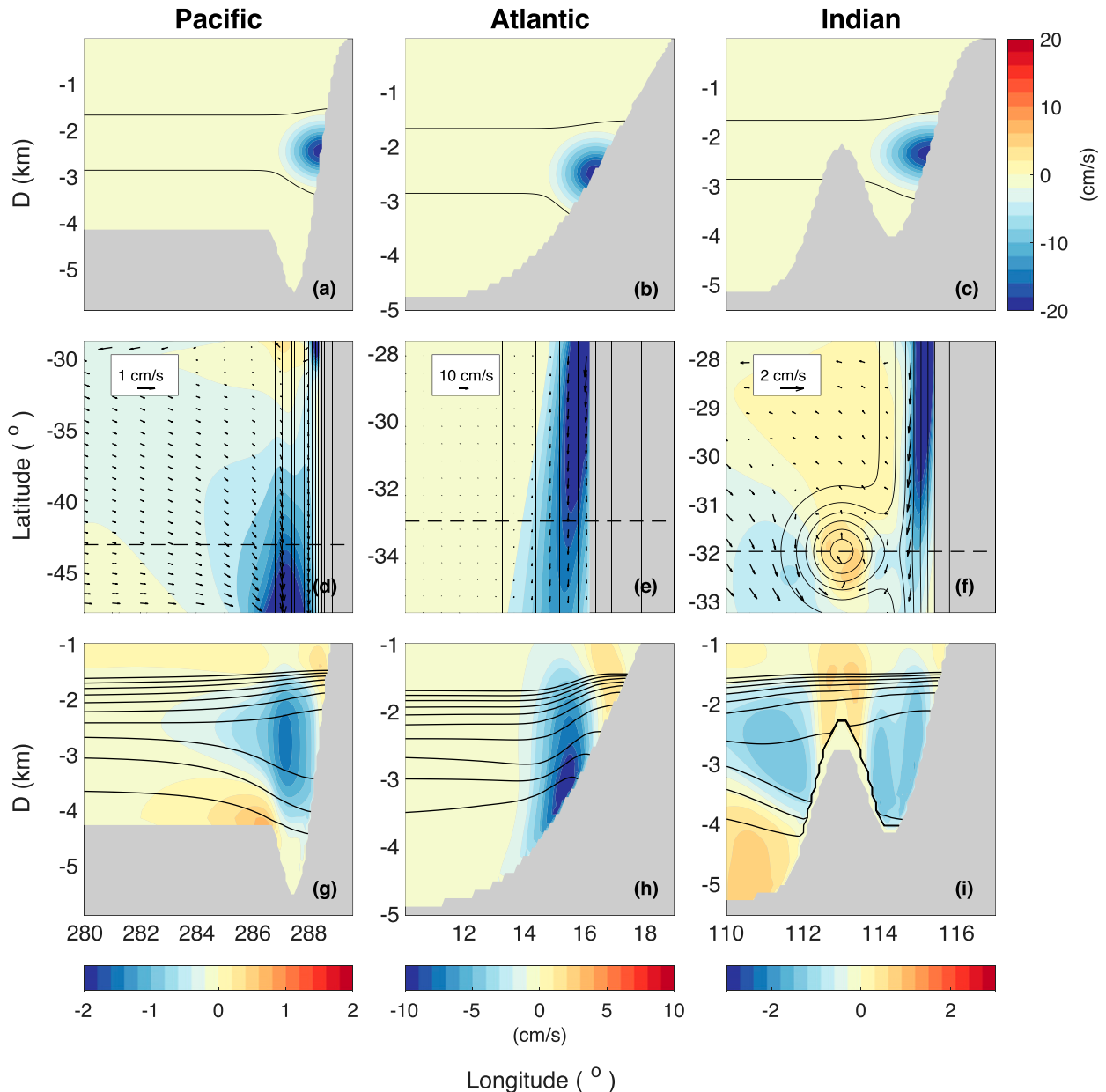


FIG. 1. Idealized MITgcm experiments for (left) the Pacific-like case, (center) the Atlantic, and (right) the Indian Ocean. (a) Pacific bathymetry (gray shading) at  $32^{\circ}\text{S}$ , inflow/outflow southward velocity (colors;  $\text{cm s}^{-1}$ ) and characteristic isotherms (black contours). (d) Meridional velocity ( $\text{cm s}^{-1}$ ) at 2.5-km depth (colors); bathymetry is shown by black contours, velocity vectors are indicated, and the dashed black line indicates the location of the zonal section in the corresponding bottom panel. (g) Zonal section of meridional velocity (color;  $\text{cm s}^{-1}$ ) and isopycnal surfaces (black contours, ranging from  $28.24$  to  $28.42 \text{ kg m}^{-3}$ , with an interval of  $0.02 \text{ kg m}^{-3}$ ). (b), (e), (h) As in (a), (d), and (g), but for the Atlantic, horizontal section taken at 2.6-km depth. (c), (f), (i) As in (a), (d), and (g), but for the Indian Ocean, horizontal section taken at 1.8-km depth.

inner edge. A no-slip boundary condition is used for the velocities at horizontal boundaries, following the realistic simulations in Yang et al. (2020a) and SOSE. The bottom boundary condition is a linear bottom drag, with a coefficient of  $10^{-3} \text{ s}^{-1}$ .

A simple linear equation of state is used ( $\rho = \rho_0[1 - \alpha(T - T_0)]$ ,  $\rho_0 = 1025 \text{ kg m}^{-3}$ ,  $T_0 = 10^{\circ}\text{C}$ , and  $\alpha = 1.668 \times 10^{-4} \text{ }^{\circ}\text{C}^{-1}$ ). The surface temperature and salinity are restored to spatially

uniform constant values (SST =  $18^{\circ}\text{C}$ , SSS = 35 psu) on a one-week time scale, and no wind forcing is applied.

For viscosity and diffusivity parameters, we first used the same coefficients as in SOSE and in the realistic regional simulations in Yang et al. (2020a), where eddies are at least partially resolved. The velocity fields of the specified inflow/outflow conditions used here should be barotropically and baroclinically

TABLE 1. Parameters in the idealized MITgcm experiments. The buoyancy frequency is that of the reference stratification profile, averaged between 2.5- and 3.5-km depth.

$A_h$ ( $\text{m}^2 \text{s}^{-1}$ )	$A_v$ ( $\text{m}^2 \text{s}^{-1}$ )	$\kappa_h$ ( $\text{m}^2 \text{s}^{-1}$ )	$\kappa_v$ ( $\text{m}^2 \text{s}^{-1}$ )	$\kappa_{\text{GM}}$ ( $\text{m}^2 \text{s}^{-1}$ )	$N^2$ ( $\text{s}^{-2}$ )	$A_4$ ( $\text{m}^4 \text{s}^{-1}$ )	$\kappa_4$ ( $\text{m}^4 \text{s}^{-1}$ )
400	$10^{-4}$	0	$10^{-5}$	200	$1.149 \times 10^{-6}$	$10^{10}$	$10^{10}$

unstable, in principle. However, in spite of the high resolution used here ( $0.1^\circ$ ), we find the Reynolds number for the DEBCs is on the order of 100, which turned out to be too small to generate energetic eddies (scaling based on  $u \sim 0.02 \text{ m s}^{-1}$ , typical for modeled DEBCs away from the sponge layers,  $L = 100 \text{ km}$  and the preliminary model horizontal viscosity used, of  $A_h = 20 \text{ m}^2 \text{ s}^{-1}$ ). Further decreases of the horizontal viscosity introduces numerical noise and even numerical instabilities. We are therefore forced to parameterize the eddy effects using a larger horizontal viscosity ( $A_h = 400 \text{ m}^2 \text{ s}^{-1}$ ), which is the smallest value that will allow the Munk layer to be resolved  $L_M \sim \sqrt[3]{A_h/\beta}$  by at least three grid points. A Gent and McWilliams (1990) diffusivity of a similar amplitude to the eddy viscosity ( $\kappa_{\text{GM}} = 200 \text{ m}^2 \text{ s}^{-1}$ ) parameterizes eddy effects in the temperature equation. The vertical viscosity  $A_v$  is  $10^{-4} \text{ m}^2 \text{ s}^{-1}$ , and the vertical diffusivity  $\kappa_v$  is  $10^{-5} \text{ m}^2 \text{ s}^{-1}$ . The trench topography, and in particular the transition from the flat interior to the trench, tends to introduce noise especially in the vertical velocity field. We later find that the vertical velocity is an essential part in the dynamics of the DEBCs (partially via topographically induced vortex stretching). Therefore, for numerical smoothness and stability, a biharmonic diffusivity and viscosity (both  $10^{10} \text{ m}^4 \text{ s}^{-1}$ ) are used [same values as in the realistic experiments in Yang et al. (2020a) and in SOSE]. A third-order direct-space-time flux-limiter advection scheme (MITgcm scheme 33) is used. All parameters are summarized in Table 1. All experiments are initialized with a reference temperature profile obtained by averaging the SOSE results along the northern edge of each domain. The models are run until a steady state is reached, which is not sensitive to the initial conditions, and the analyses are based on additional 20-yr integrations.

### b. Results of the idealized GCM configurations

In section 2b(1) we first show that the idealized configurations lead to DEBCs with similar characteristics as in SOSE and in regional realistic simulations, then in section 2b(2) discuss the sensitivity of the DEBCs' characteristics to the topographic slope width. Overall, we will see that both the results of the simulations and, more importantly, the vorticity budget of the idealized simulations are closely related to those in the realistic regional simulations of Yang et al. (2020a). This will allow us to draw conclusions on the essential elements of DEBC dynamics. When analyzing the dominant vorticity balances of the DEBC in idealized versus realistic simulations, we point out the overall similarities as well as the few significant differences that occur.

#### 1) DEBCs SIMULATED IN THE THREE IDEALIZED OCEAN BASINS

Figure 1 summarizes the structure of the DEBCs simulated in the idealized southeast Pacific/Atlantic/Indian configurations.

Concentrated southward currents are simulated in each experiment. Compared to the DEBCs simulated in the realistic regional configurations of Yang et al. (2020a), the southeast Pacific DEBC in the idealized GCM experiment is not confined to a limited latitudinal range, but starts at about  $35^\circ\text{S}$  and grows stronger southward at the specified depth of the inflow/outflow core. This difference may be related to the idealized box geometry and bathymetry, in particular, the absence of the Chile Rise (Well et al. 2003) allows the current to continue unimpeded southward along the eastern boundary. Also, the vertical section of the current (Fig. 1g) shows that the idealized DEBC has a width comparable to that of the underlying trench, while in the realistic simulations it is narrower than the trench. Despite these differences, the idealized Pacific-like DEBC is similar to the realistic one in that it is fed by semizonal flows from the west, and, on the vertical section, the core is surrounded by tilting isopycnal surfaces in thermal wind balance with the current, accompanied by a northward flow to its west. Note that the large-scale eastward flow feeding the DEBC is supported by an appropriate meridional buoyancy gradient within the western sponge layer that is not part of the physical domain.

The idealized Atlantic-like DEBC is very strong (Figs. 1e,h), with a core speed higher than  $10 \text{ cm s}^{-1}$ , and again more continuous in latitude than in the realistic simulation, and more closely attached to the eastern boundary at lower latitudes than at higher latitudes (Fig. 1e, south of  $40^\circ\text{S}$ ). A more significant difference from the realistic simulation is that the current is bottom intensified, with upward-tilting isopycnals only above the core (Fig. 1h) unlike the realistic southeast Atlantic Ocean case that shows the current to be centered at a depth of 3 km, with isopycnals tilting both below and above its core (Yang et al. 2020a). The significant momentum and vorticity transports by eddies in the Atlantic case (Yang et al. 2020a, their Fig. 10), which are missing in this idealized configuration, are very likely the reason for this difference. This is also suggested by the fact that such eddy transports have also been found to be important in driving deep southeastward flows in the interior of the southeast Atlantic by van Sebille et al. (2012). As we discuss below, the vorticity balances of the realistic and idealized Atlantic DEBCs still show strong similarities in spite of this difference in the vertical structure of the DEBC, justifying the use of the idealized configuration.

It is worth pointing out that Fig. 1 does not show the sponge layers in the north/south/west, where the open boundary conditions are forced. For all the experiments discussed in this work, a large fraction of the inflow imposed as the northern boundary condition flows westward within the northern sponge layer and then southward in the western sponge layer. Part of this flow departs from the western boundary, flows eastward and feeds the DEBCs, and the rest of this flow goes toward the

outflow boundary condition within the southern sponge layer. This means that our boundary conditions in the north and south via the sponge layers are equivalent to imposing a large-scale inflow condition from the west, or a corresponding large-scale north–south buoyancy gradient on the western boundary.

The southeast Indian-like idealized experiment shows two branches of a DEBC (Figs. 1f,i), one above the continental slope centered at 114°E and the other leaning against the western slope of the seamount, again at the depth of the core of the specified source, and compatible with observations near the Naturaliste Plateau (Toole and Warren 1993).

The consistent presence of concentrated southward flows near the eastern boundary in the idealized ocean configurations makes a strong case that these idealized experiments may be used for a better understanding of the local dynamics of these DEBCs. Also, it suggests that wind forcing and surface buoyancy gradients are not essential to the local dynamics of DEBCs. Both wind and surface buoyancy forcing, possibly at high latitudes away from the DEBC regions, are, of course, expected to play an important role in driving the deep circulation that leads to the inflows and outflows prescribed here.

## 2) SENSITIVITY OF DEBCs TO SLOPE WIDTH

The above results suggest that the DEBC width is generally comparable to the zonal scale of the bottom topography (Figs. 1g–i), motivating a study of the sensitivity to the details of the bathymetry, an appropriate goal for our idealized configurations. First, an experiment was run in which a vertical wall is used as the eastern boundary, with no trench nor slope, forced by the same inflow/outflow boundary conditions, and showed that no DEBC developed (not shown). We conclude that the bottom topography is a critical factor, and additional experiments, with different topographic slopes are therefore carried out to examine this dependence. We start with an experiment using a flat bottom (no trench) with a continental slope width of 17 km (close to the observed slope in the Pacific, blue curve in Fig. S1 in the online supplemental material), referred to as the “narrow slope” case. In the case “wide slope 1” (red) the width is 35 km, while in case “wide slope 2” the width is 70 km, and is equal to that of the observed slope used in our Atlantic cases (although the slope curvature is different, again as a sensitivity test; compare Figs. 3n,p).

The results of the narrow slope show very little concentrated flow near the eastern boundary, except very close to the northern and southern sponge layers. Most southward transport happens in the western sponge layer (which is not included in Fig. 2a), and in the interior (Fig. 2d, note that these zonal sections are 10° south of the sponge layer, so that the DEBC is well equilibrated by that point). These results agree with the “no trench” realistic case in Yang et al. (2020a). The continental slope of the narrow slope case is the same as that of the idealized Pacific case, and the only difference between them is the removal of the trench. From the fact that the DEBC does not exist in the narrow slope experiment but does appear in the idealized Pacific case (cf. Figs. 1d and 2a), we conclude that the trench is important to maintain the DEBC in the southeast Pacific Ocean.

In the wide slope 1 experiment, a strong deep concentrated southward flow develops near the eastern boundary, extending

from the northern boundary inflow to 35°S. It becomes weaker southward due to the westward flow in the same latitudinal range (Figs. 2b,e). Finally, in the wide slope 2 experiment, a DEBC that is stronger and extends farther southward is simulated (Figs. 2c,f). This implies that the bottom slope in the southeast Atlantic Ocean plays an important role in the DEBC dynamics there, similar to the trench in the Pacific Ocean.

In summary, a trench or a bottom slope are essential for a DEBC to be maintained in these experiments, and the strength and latitudinal extent of these DEBCs are both sensitive to the width of the slope. When the width is too small, a concentrated southward flow fails to develop. A wider slope leads to a DEBC that is stronger and more continuous in latitude. The role of topography is further explored below using a simpler vorticity model.

## c. Vorticity budget of the DEBCs

The following vorticity budget, evaluated at steady state, is analyzed to study the dynamics of the DEBCs:

$$u \frac{\overline{\partial \zeta}}{\partial x} + v \frac{\overline{\partial \zeta}}{\partial y} + w \frac{\overline{\partial \zeta}}{\partial z} + \beta \bar{v} = f \frac{\partial \bar{w}}{\partial z} + \hat{\mathbf{k}} \cdot \nabla \times \bar{\mathbf{F}}. \quad (1)$$

In this equation, an overbar denotes a time average,  $(x, y, z)$  are the (zonal, meridional, vertical) coordinates and  $(u, v, w)$  are the corresponding velocity components. The equation is written in Cartesian coordinates for simplicity, but the analysis is done in the spherical coordinates used by the MITgcm. The Coriolis parameter is denoted by  $f = 2\Omega \sin\theta$ , and  $\beta = 2\Omega \cos\theta/R$  is the meridional gradient of  $f$ . Finally,  $\hat{\mathbf{k}}$  is a vertical unit vector, and  $\bar{\mathbf{F}}$  is the horizontal friction force vector.

Due to the lack of surface wind and buoyancy forcing, and the weakness of the simulated DEBCs ( $\sim 3 \text{ cm s}^{-1}$ ), there is essentially no eddy activity in the simulated flow field at steady state (see discussion in section 2a). Therefore, the contribution due to resolved eddies to the nonlinear terms in Eq. (1) is negligible, and the contribution of mean flow advection is generally small as well (not shown). This is different from the results of the realistic southeast Atlantic and Indian Ocean simulations (Yang et al. 2020a).

For the idealized southeast Pacific experiment (Figs. 3a,e,i,m), it is clear that the southward flow is in the standard ocean-interior vorticity balance between stretching and planetary vorticity advection ( $\beta v \approx f w_z$ ) over most of the width of the DEBCs (west of 288°E, within the longitudinal range marked by gray shading in Fig. 3), with the friction term making a small, but not negligible, contribution in this longitudinal range. Very close to the eastern boundary, the  $\beta$  term is small due to the no-slip boundary condition and the vertical stretching and friction curl terms show strong but compensating decaying trends away from the eastern boundary. These decaying signals, trapped near the eastern boundary, are an important signature of the vorticity budget of DEBCs that appear in both the idealized and realistic simulations, as well as in SOSE, and we further explore and explain them below. We also note that the two trends change sign between 2.5- and 2-km depth (Figs. 3a,e), similar to the realistic simulations in Yang et al. (2020a), again a signature we address below. In this region, we notice

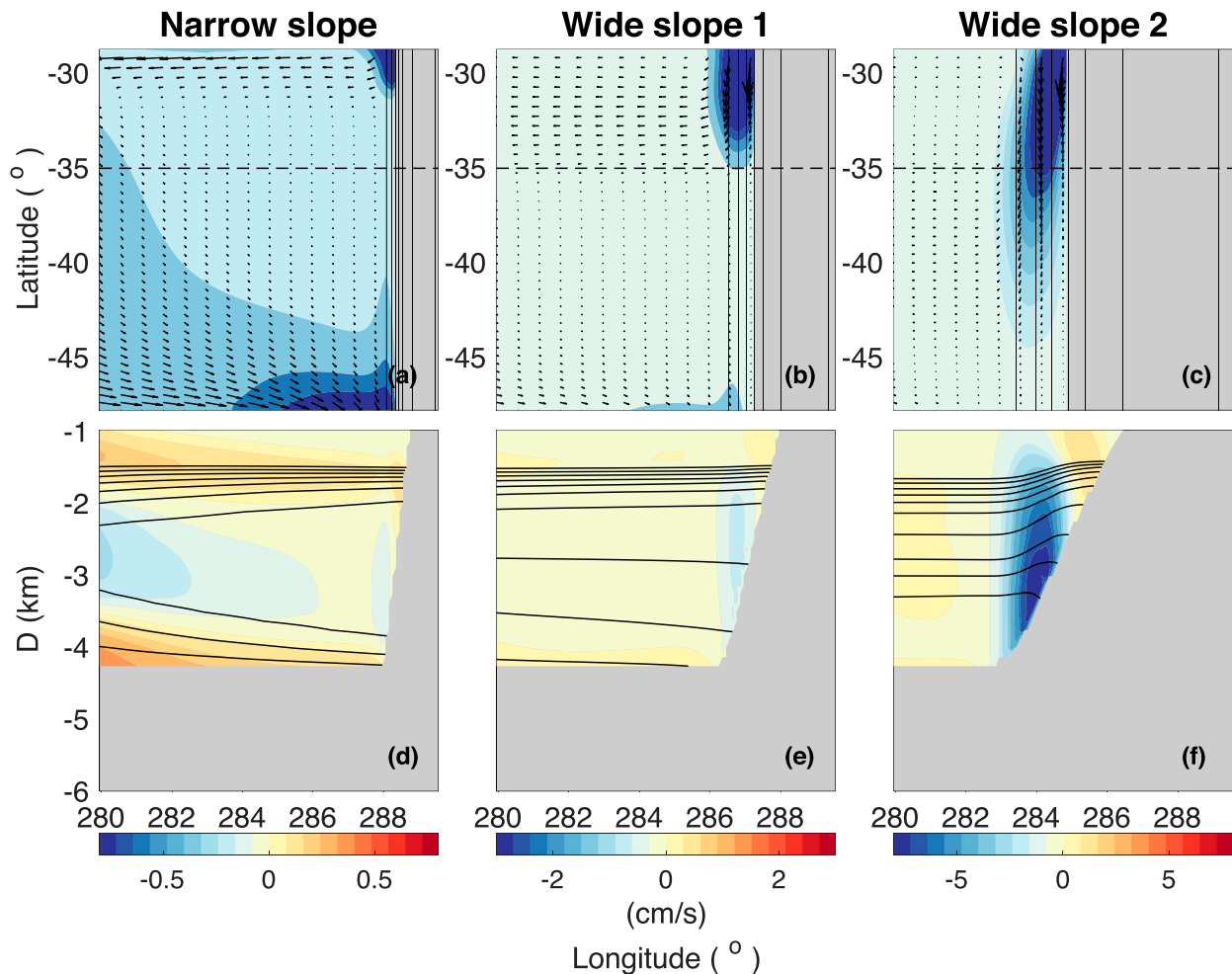


FIG. 2. Results of the sensitivity experiments with respect to the width of the continental slope (section 2). Horizontal maps are at 2.5-km depth, and zonal sections are taken at 35°S. (a) Horizontal map of northward velocity (colors;  $\text{cm s}^{-1}$ ) and velocity vectors for the “narrow slope” experiment. (d) Zonal sections of northward velocity (colors;  $\text{cm s}^{-1}$ ) and isopycnal surfaces (black contours, ranging from 28.24 to 28.42  $\text{kg m}^{-3}$ , with an interval of 0.02  $\text{kg m}^{-3}$ ). (b),(e) As in (a) and (d), but for the “wide slope 1” experiment. (c),(f) As in (a) and (d), but for the “wide slope 2” experiment.

that the stretching and friction terms are dominant but do not always fully compensate each other. This is likely due to the high order of the derivatives in these two terms, leading to a significant level of numerical errors in the evaluation of these terms from the model output, and additionally the influence of the topography in this region enhancing small-scale numerical noise in the model vertical velocity field. Very similar decaying trends are also observed in the idealized Atlantic experiment (Figs. 3b,f,j,n) and in the wide slope experiment (Figs. 3d,h,l,p).

A similar vorticity balance of vertical stretching (shown in the temperature budget below to be mostly forced by parameterized horizontal buoyancy mixing in this region, section 3a) and horizontal friction very close to the eastern boundary has been discussed in the context of linear circulation in rotating stratified fluids (Barcilon and Pedlosky 1967; LaCasce 2004; Gjermundsen and LaCasce 2017). In these theories, the purpose of this frictional sublayer is to satisfy the no parallel flow condition along the boundary, consistent with the case here.

Similarly, Bire and Wolfe (2018) find such a balance in their treatment of upper ocean eastern boundary currents.

In the idealized Indian Ocean experiment (Figs. 3c,g,k,o), we again observe the strongly decaying trends at the core of the current at 2.5-km depth and below, very close to the eastern boundary. Because of the more complicated bottom topography (which includes a seamount), there is more structure in each term than in the other idealized cases, and the interior vorticity balance is not as clear in this case. At 3-km depth in the Indian Ocean, we observe the decaying signals occur at two longitudinal locations, one just west of the seamount and the other very close to the eastern boundary, reinforcing the idea that the DEBC is split into two branches.

The fact that over most of the longitudinal range of the southward DEBC the current is in the ocean-interior vorticity balance means that these currents are dynamically different from Munk-type western boundary currents, which are governed by a different vorticity balance (although see

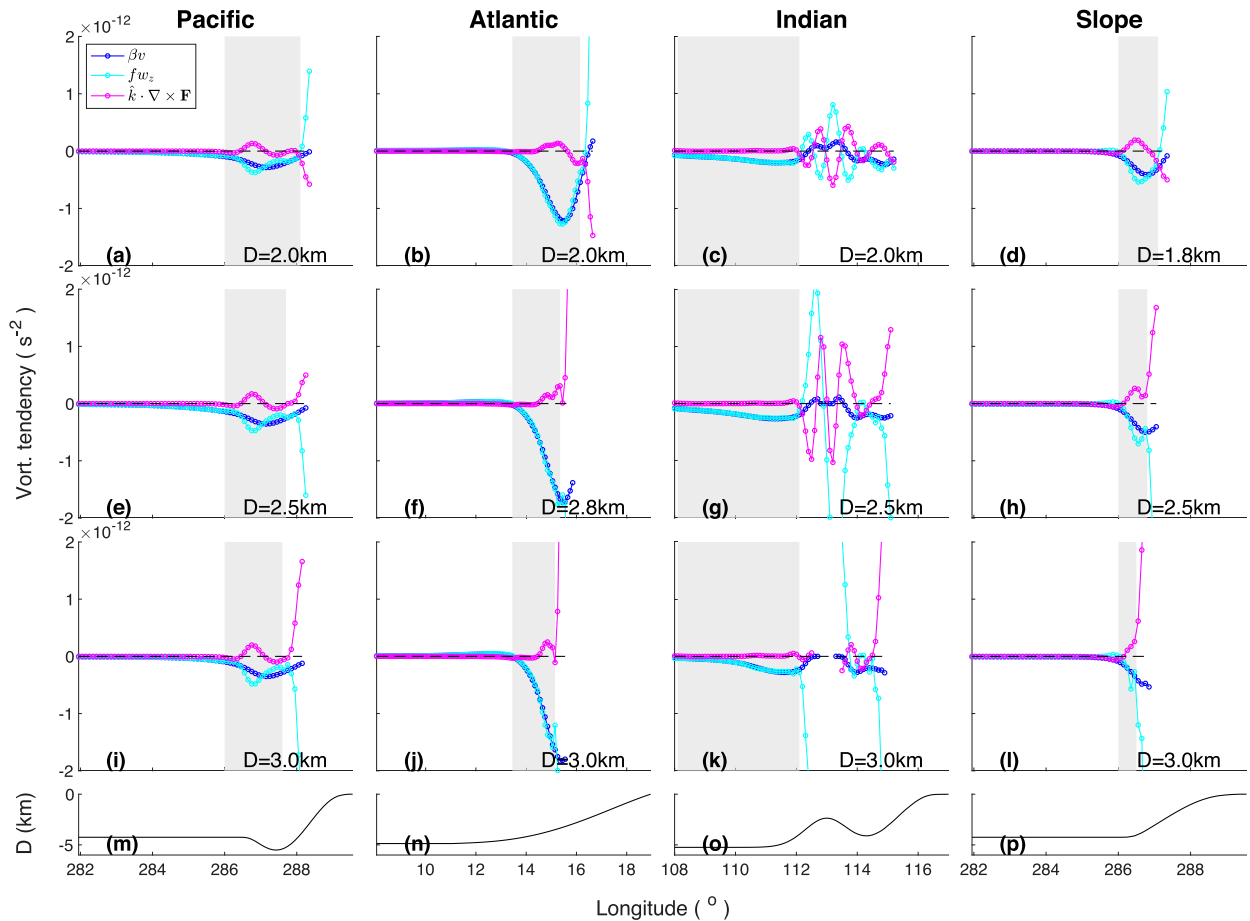


FIG. 3. Vorticity budgets of the idealized GCM experiments, at different levels, with the gray shading indicating the region where  $\beta v \approx f w_z$  is the dominant balance. (a),(e),(i) Pacific, at 2-, 2.5-, and 3-km depth, at 46°S. (m) The corresponding bathymetry profile. (b),(f),(j),(n) As in (a), (e), (i), and (m), but for the Atlantic, at depths of 2-, 2.8-, and 3.0-km depth, 33°S. (c),(g),(k),(o) As in (a), (e), (i), and (m), but for the Indian-like case, at depths of 2.0-, 2.5-, and 3.0-km depth, at 32.15°S. (d),(h),(l),(p) As in (a), (e), (i), and (m), but for the “wide slope 1” case, at depths of 1.8-, 2.5-, and 3.0-km depth, at 33°S.

Hughes and De Cuevas 2001). While the linear vorticity budget does not close as well very near the eastern boundary because friction term involves higher derivatives and numerical errors in the evaluation of these terms are magnified, the presence of the decaying signals of stretching and friction is robust.

**3. A simple vorticity model**

The dynamics over most of the width of the DEBCs simulated in the idealized GCM configurations are mostly governed by vortex stretching above a variable-depth bathymetry, while very close to the eastern boundary the balance is between the decaying trends of friction and stretching away from the eastern boundary [as discussed in contexts different from ours by Barcilon and Pedlosky (1967), LaCasce (2004), Gjermundsen and LaCasce (2017), Bire and Wolfe (2018), Wolfe and Bire (2019), and Bire (2019)]. To evaluate the role and importance of each process in the DEBC dynamics, and further understand different features of the GCM solutions, a simplified linearized vorticity model that is motivated by the GCM results is

now developed and analyzed. It should be clear that this simple model is not meant as an attempt at a rigorous solution of stratified linear dynamics (Barcilon and Pedlosky 1967; LaCasce 2004; Gjermundsen and LaCasce 2017). Instead, it is based on heuristic assumptions allowing us to further understand the realistic and idealized GCM results.

In the following subsections we first (section 3a) derive the vorticity equation. Then, in section 3b, we examine its asymptotic behavior near the eastern boundary and thus explain the vertical structure of the vorticity balances seen in the GCMs. Section 3c employs a crude approach to incorporating the role of topography by vertically integrating the vorticity equation and is thus able to consider the effects of both stratification and topography.

*a. Model derivation*

Having observed the important role of the vertical velocity in the DEBCs dynamics, via the stretching term, we consider first the temperature budget that allows us to express the vertical velocity in terms of the temperature,

$$\bar{\mathbf{u}}_h \cdot \nabla_h \bar{T} + \overline{\mathbf{v}' \cdot \nabla T'} + \bar{w} \frac{N^2}{\alpha g} = \text{diff}. \quad (2)$$

Here,  $\bar{(\cdot)}$  denotes time average and  $(\cdot)'$  departure from time average. The horizontal velocity vector is  $\mathbf{u}_h$ ,  $\mathbf{v}$  is the 3D velocity vector,  $\nabla_h$  is the horizontal gradient operator,  $\nabla$  is the 3D gradient operator,  $w$  is the vertical velocity,  $T$  is the temperature,  $N^2 \equiv -g\bar{\rho}_z/\rho_0 = \alpha g \bar{\partial T}/\partial z$  is the vertical stratification,  $\alpha$  is the thermal expansion coefficient, and  $g$  is the gravitational acceleration. Finally, diff is the total tendency due to parameterized eddy mixing (diffusion).

Using (2) we decompose the vertical velocity into three components due to: mean flow advection, eddy advection and parameterized eddy mixing. As there is no explicit eddy activity in the idealized GCM experiments, the contribution by resolved eddy advection is very small. In Yang et al. (2020a) we found that the eddy temperature advection is important in the southeast Atlantic and Indian simulations. That contribution is parameterized in the above idealized experiments by the larger eddy diffusivity (section 2a). For the idealized Pacific experiment, advection by the mean flow is also not important in the DEBC region, where vertical velocity is dominated by parameterized horizontal eddy mixing (Figs. 4a–d). For the idealized Atlantic case, the narrow upwelling band in the eastern segment of the DEBC is again driven by parameterized horizontal eddy mixing (Figs. 4e,g,h). Away from the DEBC region the vertical velocity is dominantly driven by mean flow advection, due to the westward flow (not shown) down the isopycnal slope (Fig. 1h). Similarly, in the idealized Indian Ocean experiment (Fig. 4), the pattern of the vertical velocity is mainly governed by parameterized eddy mixing.

In summary, the buoyancy budget suggests that the contribution by nonlinear mean and eddy advection is negligible in the Pacific, but not in the other ocean basins. For the sake of simplicity, however, we will only consider a linear buoyancy equation in our simple model, and use a larger eddy diffusivity to represent eddy effects, replacing the along-isopycnal Gent–McWilliams diffusion with a simpler horizontal and vertical diffusion formulation. As we will see, the vorticity budget of the simple model captures the main signals seen in the GCM experiments and leads to additional insights in spite of the approximations taken, justifying the use of the linearized temperature budget.

The starting point dynamical equations are, therefore,

$$\begin{aligned} -fv &= -\frac{1}{\rho_0} \frac{\partial p}{\partial x}, \\ fu &= -\frac{1}{\rho_0} \frac{\partial p}{\partial y} + A_h \nabla_h^2 v + A_v \frac{\partial^2 v}{\partial z^2}, \\ \frac{\partial p}{\partial z} &= -\rho g, \\ \rho &= -\alpha \rho_0 T, \\ w \frac{N^2}{\alpha g} &= \kappa_h \nabla_h^2 T + \kappa_v \frac{\partial^2 T}{\partial z^2}, \end{aligned} \quad (3)$$

where  $A_{h(v)}$  is the horizontal (vertical) viscosity and  $\kappa_{h(v)}$  is the horizontal (vertical) diffusivity. This is the semigeostrophic

approximation, and it is justified by noting that the friction terms in the  $u$  momentum equation (first line above) are negligible in our GCM vorticity balance. Taking the curl of the momentum equations and replacing the vertical velocity in the stretching term with that from the buoyancy equation, we get

$$\beta v = \frac{\alpha g f}{N^2} \frac{\partial}{\partial z} \left( \kappa_h \nabla_h^2 T + \kappa_v \frac{\partial^2 T}{\partial z^2} \right) + \left( A_h \nabla_h^2 + A_v \frac{\partial^2}{\partial z^2} \right) \frac{\partial v}{\partial x}. \quad (4)$$

We then introduce a streamfunction  $\psi$  such that  $u = -\partial_y \psi + (A_h \nabla_h^2 + A_v \partial_{zz}) \partial_x \psi / f$  and  $v = \partial_x \psi$ , and  $T = f \psi_z / (\alpha g)$ . Therefore, (4) can be written in terms of the streamfunction as

$$\beta \frac{\partial \psi}{\partial x} = \frac{f^2}{N^2} \frac{\partial^2}{\partial z^2} \left( \kappa_h \nabla_h^2 \psi + \kappa_v \frac{\partial^2 \psi}{\partial z^2} \right) + A_h \nabla_h^2 \frac{\partial^2 \psi}{\partial x^2} + A_v \frac{\partial^2}{\partial z^2} \frac{\partial^2 \psi}{\partial x^2}. \quad (5)$$

A nearly identical semigeostrophic vorticity equation has been derived and studied by McCreary et al. (1986) and Bire and Wolfe (2018), for the pressure field. The closed form Eq. (5) for the streamfunction is next used to further understand some of the vorticity signatures of the DEBC found in the GCM results.

Our first objective is to use the vorticity Eq. (5) in order to explain 1) the decaying trends of friction and stretching seen in the vorticity budgets of the realistic and idealized GCM experiments and 2) the change of sign of these decaying trends with depth, as seen in Fig. 3. For this purpose, consider a flat bottom case and decompose the streamfunction into vertical modes in the form of  $\cos(\pi m z / H)$ , in which  $m$  is the vertical wavenumber and  $H$  is the total depth of the ocean. The form of the modes is chosen such that each mode satisfies vertical boundary condition  $b = 0$ ,  $b_{zz} = 0$  at  $z = 0, -H$  (McCreary et al. 1986; Wolfe and Cessi 2009). An analysis of the vertical structure of the DEBCs of the realistic *regional Atlantic*, *regional Indian*, and *regional Pacific* simulations in Yang et al. (2020a), shows that these currents generally have a Gaussian-like vertical structure. Therefore, in this simple vorticity model, we also attempt to impose a Gaussian vertical structure on the streamfunction,  $G(z) = \exp[-(z - z_0)^2 / \sigma^2]$ . To do so, write  $G(z) = \sum_{m=0}^M a_m \cos(\pi m z / H)$ , where 12 modes are sufficient to precisely reconstruct the Gaussian structure (Fig. S2a) for  $H = 4$  km,  $z_0 = -2.5$  km and  $\sigma = 500$  m. Next, we expand the streamfunction in terms of horizontal structure functions  $\phi_m(x, y)$  and vertical modes,

$$\psi(x, y, z) = \sum_{m=0}^M \phi_m(x, y) a_m \cos(\pi m z / H). \quad (6)$$

As we will see below, because the horizontal structure functions  $\phi_m$  depend on the vertical wavenumber  $m$ , the vertical structure ends up being only approximately Gaussian. This suffices for the purpose of the analysis here, which does not aim to provide a full solution of the linearized equation, or a rigorous solution for the entire domain, but focuses on understanding the decay scales from the eastern boundary and the vorticity budget in the regional MITgcm model results. As we will show in the following, this toy model, although based on significant idealizations, successfully explains the vorticity dynamics of the GCM results (Fig. 3). It also enables us to identify

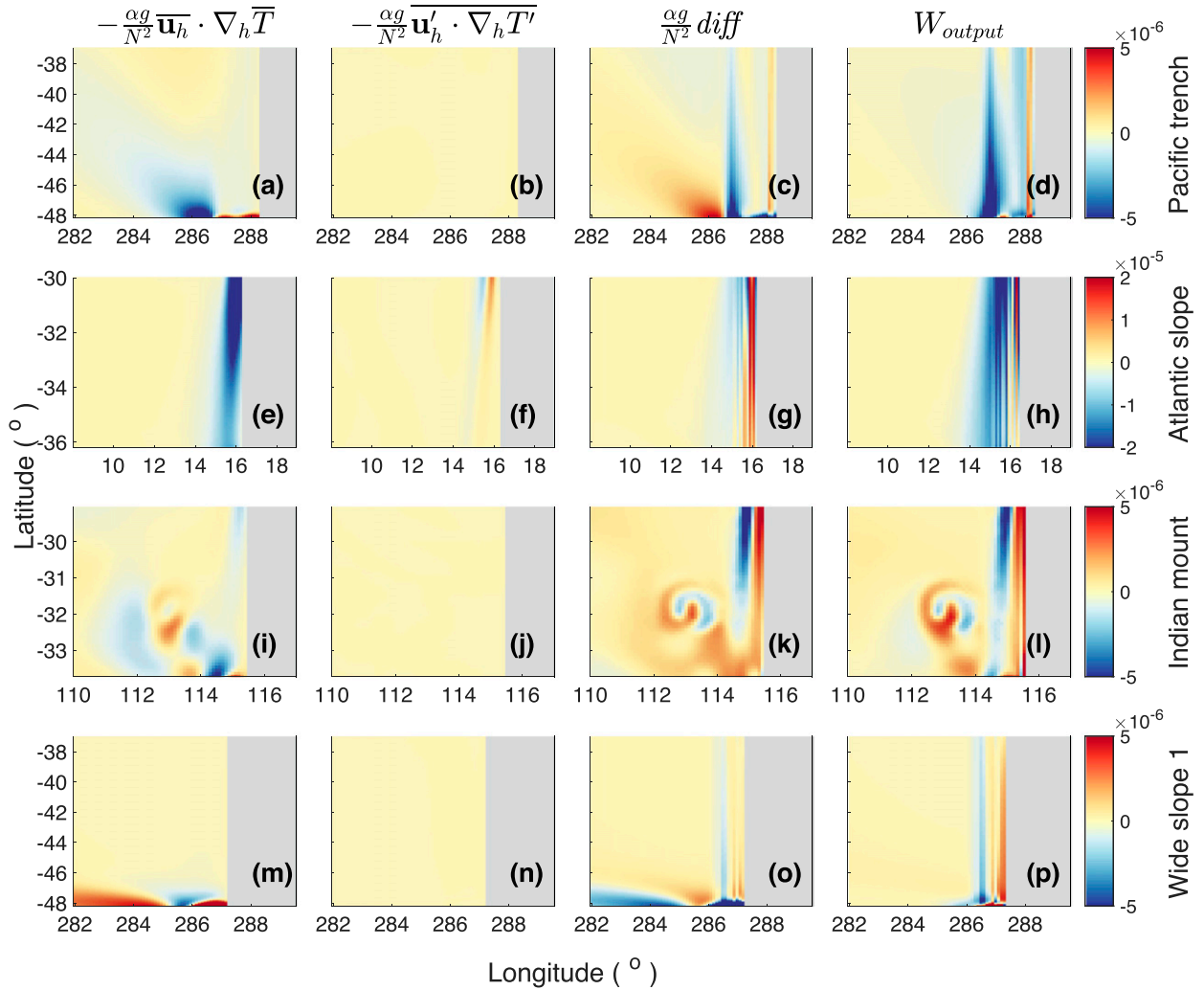


FIG. 4. Reconstructing the vertical velocity ( $\text{m s}^{-1}$ ) in the idealized MITgcm experiments from different terms in the temperature equation. (a)–(c) Mean flow advection, eddy advection, and parameterized mixing, correspondingly, at 2.5-km depth, Pacific case. (d) Actual GCM vertical velocity in the same idealized Pacific case, at 2.5-km depth. (e)–(h) As in (a)–(d), but for the idealized Atlantic case, at 2.5-km depth. (i)–(l) As in (a)–(d), but for the idealized Indian-like case, at 1.6-km depth. (m)–(p) As in (a)–(d), but for the “wide slope 1” case, at 2.5-km depth.

parameterized eddy mixing of temperature and topography as two important contributors to the vertical stretching that drives the DEBC, as discussed in section 3c.

*b. Eastern boundary solutions*

For each vertical wavenumber  $m$ , Eq. (5) becomes

$$A_h \nabla_h^2 \frac{\partial^2 \phi_m}{\partial x^2} - \left(\frac{\pi m}{H}\right)^2 \left(\frac{f^2}{N^2} \kappa_h \nabla_h^2 + A_v \frac{\partial^2}{\partial x^2}\right) \phi_m - \beta \frac{\phi_m}{\partial x} + \left(\frac{\pi m}{H}\right)^4 \frac{f^2}{N^2} \kappa_v \phi_m = 0. \tag{7}$$

To identify solutions of (7) that decay from the eastern boundary, we assume that the  $x$  derivatives dominate the  $y$  derivatives based on the structure of the DEBC, and let  $\phi_m$  have an exponential form in  $x$ , as  $\phi_m \sim \exp(K_m x)$ , allowing  $K_m$

to be complex. Equation (7) becomes a polynomial equation for the zonal wavenumber  $K_m$ ,

$$A_h K_m^4 - \left(\frac{\pi m}{H}\right)^2 \left(\frac{f^2}{N^2} \kappa_h + A_v\right) K_m^2 - \beta K_m + \left(\frac{\pi m}{H}\right)^4 \frac{f^2}{N^2} \kappa_v = 0. \tag{8}$$

Solving Eq. (8) using the same parameters as used in the idealized GCM experiments, we find that this equation has two roots for each vertical mode  $m$ , whose real parts are positive (solutions decaying from the eastern boundary) and two roots whose real parts are negative (solutions decaying from the western boundary). We focus on the eastern boundary solutions. Figure 5a shows the dependence of the two length scales on the vertical mode number. We first notice that the two length scales corresponding to the eastern boundary modes are

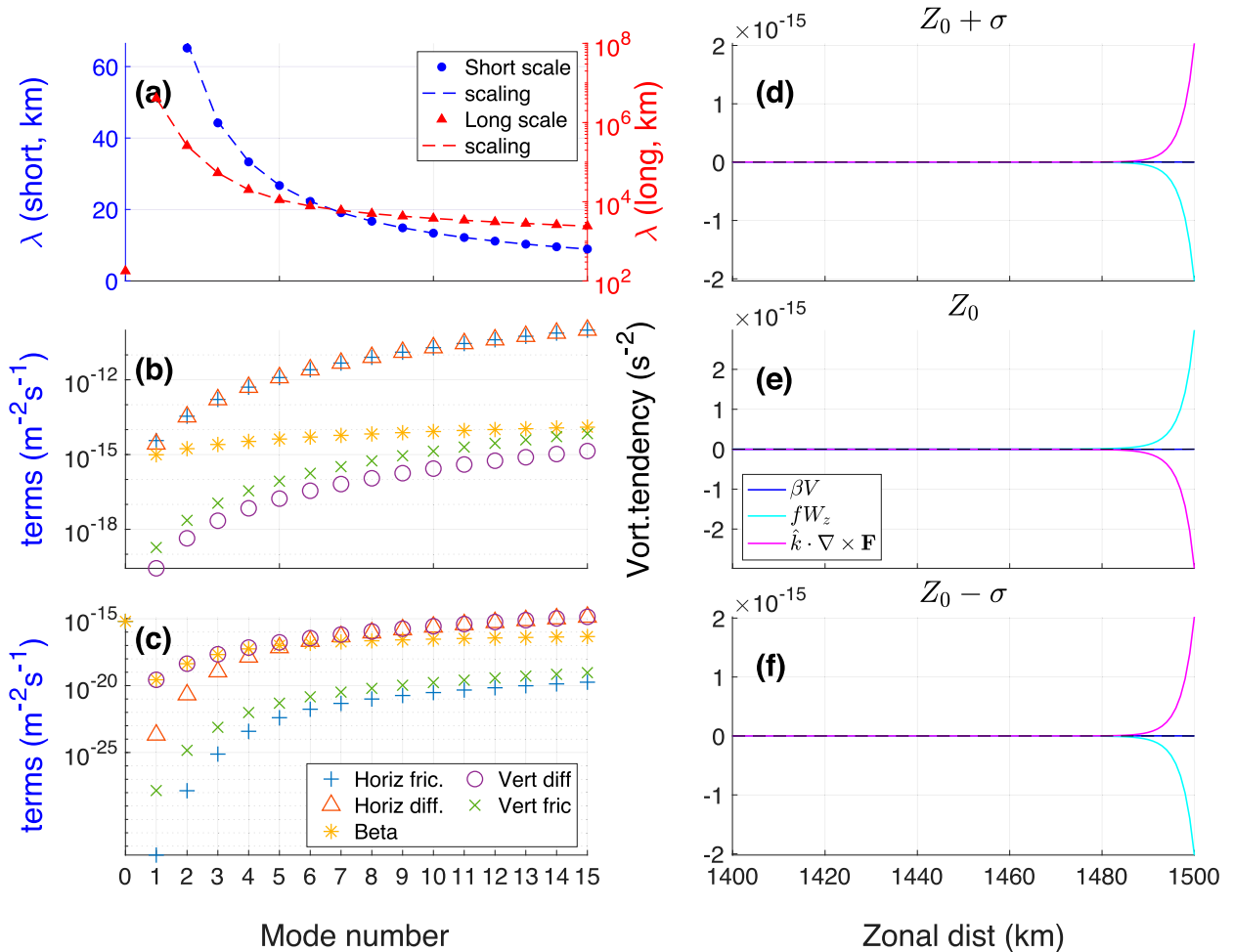


FIG. 5. Demonstrating the presence and the vorticity dynamics of the small and large decay scales from the eastern boundary, and the change of signs of vorticity trends in the vertical, seen in the GCM results of Fig. 3. (a) The dependence of the short length scale of the eastern boundary decaying modes on the vertical wavenumber [derived from Eq. (8), shown by blue dots, left axis]; similarly, the long scale is shown by red triangles (and right axis), and the scaling for the length scales is shown by dashed lines (see text). (b) The magnitude of each term in the vorticity Eq. (8) for the short-wavelength solution. (c) The magnitude of each term of the long-wavelength solution. (d)–(f) The three-term vorticity balance at different depths (only the easternmost 100 km are shown): (d)  $z_0 + \sigma$ , (e)  $z_0$ , and (f)  $z_0 - \sigma$ .

well separated when using the GCM parameters, with the short length scale ranging from 15 to 65 km, and the long one ranging from 100 to 1000000 km. The long length scale becomes smaller, on the order of  $10^2$  km, for very high vertical wavenumber modes, whose contribution to the solution is small. Given that Laplacian friction is used, two boundary conditions need to be satisfied at each horizontal boundary: no normal flow and no slip, as is the case in the Munk model for western boundary layers. This requires two decaying modes near the boundary, and the fact that we have effectively just one such eastern boundary mode (the other having a very long decay scale) means that the eastern boundary cannot support two such conditions and the no-normal flow must be satisfied by the interior solution. This implies that the deep eastern boundary current is not a boundary current in the same sense as the Munk-type western boundary current in the Munk model, whose two decaying modes from the western boundary have

comparable zonal decaying scales and thus can satisfy both the no-flow and no-slip boundary conditions (Munk 1950; Pedlosky 1987).

We can now examine the terms in the vorticity Eq. (5) for each of the two decaying modes as functions of the vertical mode number  $m$ . Figures 5b and 5c show the magnitude of different terms in Eq. (8) as functions of vertical mode number, for the short- and long-scale decaying solutions. Figure 5b shows that the dominant balance of the short-scale solution, which is relevant to the strong decaying trends observed in the GCM, is between horizontal friction and horizontal diffusion (i.e., parameterized eddy viscosity and eddy mixing) for all vertical mode numbers. This is the same balance as the “hydrostatic layer” discussed in Barcelon and Pedlosky (1967), Pedlosky (2003), and Bire and Wolfe (2018). For the long-scale eastern-boundary solution (Fig. 5c), for  $m = 0$  (representing a uniform vertical structure), the balance is the standard Munk

western-boundary balance between horizontal friction and the  $\beta$  term. For  $m = 1$ , the dominant balance is between  $\beta$  term and vertical stretching forced by vertical heat diffusion, similar to the balances discussed in McCreary et al. (1986), Tziperman (1987), and Kawase (1987). This is the standard ocean-interior vorticity balance ( $\beta v \approx f w_z$ ). For vertical wavenumbers higher than one, the contribution of horizontal diffusion becomes more important and counteracts the effect of the vertical diffusion. The residual of the horizontal and vertical diffusion is balanced by the  $\beta$  term.

It is now possible to estimate the short and long length scales of the solutions decaying from the eastern boundary, based on the above balances. For the short length scale, the dominant balance is  $A_h K_s^2 \sim (\pi m/H)^2 f^2 \kappa_h / N^2$ . Therefore, the corresponding length scale is

$$L_s = \frac{2\pi}{K_s} = \frac{2H}{m} \sqrt{\frac{N^2 A_h}{f^2 \kappa_h}}. \tag{9}$$

The short length scale is proportional to the Rossby deformation radius and the square root of the Prandtl number, and is inversely proportional to vertical wavenumber. Similarly, the long length scale can be found by assuming a three term balance of horizontal diffusion, vertical diffusion and  $\beta$  terms (not shown).

Our next objective is to understand the vertical structure of the eastern boundary vorticity balances shown in Fig. 3 using the solution of the simple vorticity equation as function of  $x$  and  $z$ . Specifically, we are interested in the sign change of the dominant terms near the eastern boundary, when evaluated below and above the core of the DEBC (see magenta and cyan lines in Fig. 3). Start with the horizontal structure  $\phi_m(x)$  for each vertical mode. For a single vertical mode  $m$ , the zonal structure of  $\phi_m$  is  $\phi_m = c_m \exp(K_{m1}x) + d_m \exp(K_{m2}x)$ , in which  $K_{m1}$  is the high wavenumber (short length scale) and  $K_{m2}$  is the low wavenumber, and therefore  $K_{m1} \gg K_{m2}$ . In order for the streamfunction to have the assumed Gaussian structure on the eastern boundary,  $x = L$ , Eq. (6) requires that  $\phi_m = 1$  there. Using also a no-parallel-flow boundary condition on the eastern boundary, imposed by requiring  $\partial_x \phi_m(x = L) = 0$ , we find,

$$\begin{aligned} \phi_m = & \frac{K_{m2}}{K_{m2} - K_{m1}} \exp[K_{m1}(x - L)] \\ & - \frac{K_{m1}}{K_{m2} - K_{m1}} \exp[K_{m2}(x - L)]. \end{aligned} \tag{10}$$

The full 3D solution of streamfunction is now,

$$\begin{aligned} \psi(x, z) = & \sum_{m=0}^M \left[ \frac{K_{m2}}{K_{m2} - K_{m1}} e^{K_{m1}(x-L)} - \frac{K_{m1}}{K_{m2} - K_{m1}} e^{K_{m2}(x-L)} \right] \\ & \times a_m \cos\left(\frac{\pi m z}{H}\right). \end{aligned} \tag{11}$$

We can now finally see that the solution to the simple vorticity equation, given in Eq. (11), has a similar vertical structure of the vorticity balance as observed in the GCM (Fig. 3). Plugging (11) into the vorticity Eq. (5), we calculate each term in the vorticity budget as functions of  $x$  and  $z$ . The dominant terms in

the narrow boundary vorticity balance (horizontal friction and horizontal diffusion, shown by magenta and cyan lines in Figs. 5d,e,f) change sign between different layers, as observed in the GCM (e.g., Figs. 3d,h,i). The  $\beta v$  term is much weaker in this analysis, due to the missing but important role played by bathymetry, as discussed later.

We note that the solution (11) is exactly Gaussian at the eastern boundary by construction, but deviates from that slightly away from the eastern boundary due to the dependence of  $K_{m1}$  and  $K_{m2}$  on the vertical wavenumbers. However, the solution is still approximately Gaussian all the way to at least 2000 km from the eastern boundary, as seen in Fig. S2b, thus justifying our ansatz.

We have also explored the sensitivity of the two length scales of solutions decaying from the eastern boundary over a broad parameter regime, by changing the physical parameters ( $A_h$ ,  $\kappa_h$ ,  $\kappa_v$ ,  $A_v$ , and  $N^2$ ) from 0.01 to 100 times of their reference values (those used in the idealized GCM experiments), as shown and discussed in the online supplementary information. One noteworthy result is that the long scale rapidly decreases with an increasing vertical diffusivity, allowing an eastern-boundary trapped current as discussed in Tziperman (1987), McCreary et al. (1986), Kawase (1987), Weaver and Middleton (1989), and Park (2006).

### c. Vertically integrated simple vorticity model

The GCM results demonstrate the important role played by topography and stratification in forcing the vertical stretching term which drives much of the DEBC flow. The GCM does not allow us to separate these two effects, and we therefore attempt to further explore this issue using the simple vorticity model derived above. The analysis in this section should again not be viewed as an attempt at a rigorous solution of the linearized dynamics (Barcilon and Pedlosky 1967; LaCasce 2004; Gjermundsen and LaCasce 2017). Instead, this is meant as a heuristic analysis allowing us to further understand the realistic and idealized GCM results. For this purpose, we integrate the vorticity model vertically, from  $z_0 - \sigma$  to  $z_0 + \sigma$ . We make the (unrealistic) assumption that the ocean bottom boundary condition may be applied at  $z_b = z_0 - \sigma$ , that is, below the peak of the prescribed Gaussian vertical structure of the horizontal velocity field. In this way the horizontal flow is nonnegligible at the depth of the topography, which guarantees that the topography interacts with the horizontal flow, as clearly seen in the above GCM solutions. Furthermore, in the same spirit of idealization, the bottom boundary condition is linearized by assuming topographic deviations to be small, so we can impose the bottom boundary condition  $w(z_b) = -u(z_b) \partial_x h$  at a single depth of  $z_b = z_0 - \sigma$ . The underlying assumption that the topographic disturbances are smaller compared to the average depth of the ocean is again not particularly realistic, especially very close to the eastern boundary, but we note that most of the width of the GCM-simulated DEBCs that are in the interior-like vorticity balance is separated from the steep slopes where this assumption is strongly violated. As we will show later, this idealization gives realistic-looking solutions of DEBCs forced by topography and provides useful insights, demonstrating the value of this simple model.

## 1) DERIVATION

Using again the decomposition  $\psi(x, y, z) = \phi(x, y)G(z)$  with the assumed Gaussian vertical structure  $G(z)$ , we find,

$$\begin{aligned} & \left( A_h \nabla_h^4 \phi + \beta \frac{\partial \phi}{\partial x} \right) \int_{z_0 - \sigma}^{z_0 + \sigma} G(z) dz + A_v \nabla_h^2 \phi G'(z) \Big|_{z_0 - \sigma}^{z_0 + \sigma} \\ & + \frac{f^2}{N^2} [\kappa_h \nabla_h^2 \phi G'(z) + \kappa_v \phi G'''(z)] \Big|_{z_0 + \sigma} \\ & - \frac{\partial \phi}{\partial y} G(z_0 - \sigma) \frac{\partial h}{\partial x} = 0. \end{aligned} \quad (12)$$

Here,  $G'$  and  $G'''$  are the first and third derivatives of the Gaussian structure, the first of the four terms shown above is the sum of the horizontal friction and the  $\beta$  term, and the balance between these two terms is the western boundary balance in the standard Munk model. The second term is the contribution of vertical friction (negligible in the reference parameter regime used in the idealized GCM runs). The third term is the stretching due to the vertical velocity evaluated at  $z_0 + \sigma$  using the buoyancy equation, representing the effects of parameterized temperature mixing. The last term is the stretching due to the bottom vertical velocity, which is evaluated using the bottom boundary condition, representing the topographic stretching.

The equation is forced by inflow/outflow boundary conditions similar to those used in the GCM simulations, with a Gaussian structure in longitude. No-flow boundary conditions are used on the western and eastern boundaries. This simple vorticity model is not designed to resolve eddies explicitly. The lack of eddies is in accordance with the idealized GCM simulations and, as will be shown later, this eddy-free simple model can still give results that reveal the most important aspects of the local vorticity dynamics of the DEBCs. The model is solved numerically in a 1000 km  $\times$  2000 km horizontal domain in the (east, north) directions, using a 5-km resolution horizontal grid. The solution is obtained by writing the finite difference version of the above equation in matrix form, and solving it using MATLAB.

## 2) RESULTS

We solve the full integrated vorticity model (12) forced by different bathymetry configurations: “trench” (using bathymetry from the idealized GCM Pacific experiment), “slope” (Atlantic), and “flat bottom.” Figures 6a, 6f, and 6k show the results of the trench Pacific-like case. Figure 6a shows a clear DEBC whose width is obviously confined to the region of varying bottom topography (Fig. 6k). The DEBC grows stronger southward, being fed by an eastward flow. Its vorticity budget (Fig. 6f) shows similarities to that of the idealized Pacific GCM experiment (Fig. 3i), with an interior-like balance over the western flank of the trench, and decaying trends near the boundary.

The vortex stretching term, due to the integrated form of  $f w_z$  is written in Eq. (12) explicitly in terms of the effect of the bottom topography and of the temperature diffusion. This allows us to find that the both the topography and parameterized temperature eddy mixing contribute significantly to the

stretching, although a quantitative estimate of the two terms is not possible given the many idealizations used.

In the flat bottom case (Figs. 6b,g,l), no DEBC appears in the solution and the inflow is directed to the western boundary. This is consistent with the similar flat-bottom GCM result mentioned above and confirms the important role of topography, and the integrated vorticity model allows us to identify that it serves as an important source of vortex stretching. In the Atlantic-like slope case (Figs. 6e,j,o), the southward flow above the slope is also very wide due to the width of the topography, and it loses its boundary current character. This discrepancy between the simple vorticity model and the realistic regional GCM results is probably due to the missing role of eddies in the Atlantic discussed in Yang et al. (2020a) (see also van Sebille et al. 2012; Bire and Wolfe 2018). However, its vorticity budget is still very similar to that in the idealized Atlantic GCM experiment (Fig. 3j).

The sensitivity to the width of the slope and to the height of the topography are studied in Fig. 7. We find that using a steeper slope configuration, while keeping the slope width constant (Figs. 7c,h,m) leads to a more extended DEBC, starting from the source region southward. When the slope width is modified, leaving the slope angle constant (Figs. 7e,j,o), a wider slope allows a more southward extended DEBC to develop.

We proceed to study the role of stratification in the DEBC dynamics, where again the vorticity model allows a deeper understanding than is possible with the GCM experiments alone. The “Munk trench” case shown in Figs. 6c, 6h, and 6m is the same as the trench case, but without stratification: in Eq. (12) the terms involving  $A_v$ ,  $\kappa_v$ , and  $\kappa_h$  are set to zero. This case does show a concentrated southward flow above the trench (Figs. 6c,h,m), but the vorticity budget is very different from that seen in the standard vorticity model (Figs. 6a,f,k) or the GCM results, as it lacks the trapped compensating decaying trends in friction and stretching near the eastern boundary. This indicates that stratification is critical for the DEBC dynamics near the boundary, consistent with the linear stratification theory of Barcilon and Pedlosky (1967). Next, consider the Munk case, where we have now eliminated both stratification and topography. This case recovers the standard Munk western boundary current where the  $\beta$  term and horizontal friction balance each other, as expected.

## 4. Conclusions

This paper continues the study of the dynamics of deep eastern boundary currents by Yang et al. (2020a), where realistic simulations were used to study the vorticity dynamics of DEBCs in the South Pacific, Atlantic, and Indian Oceans. In this work, we use idealized GCM configurations to identify the essential ingredients responsible for driving DEBCs. Based on the results of the idealized GCM experiments, we develop a semianalytical simple vorticity model. We use this simple model to study the vorticity balances as function of longitude and depth, and use its vertically integrated version to study the role of bottom topography and stratification in the dynamics of these currents.

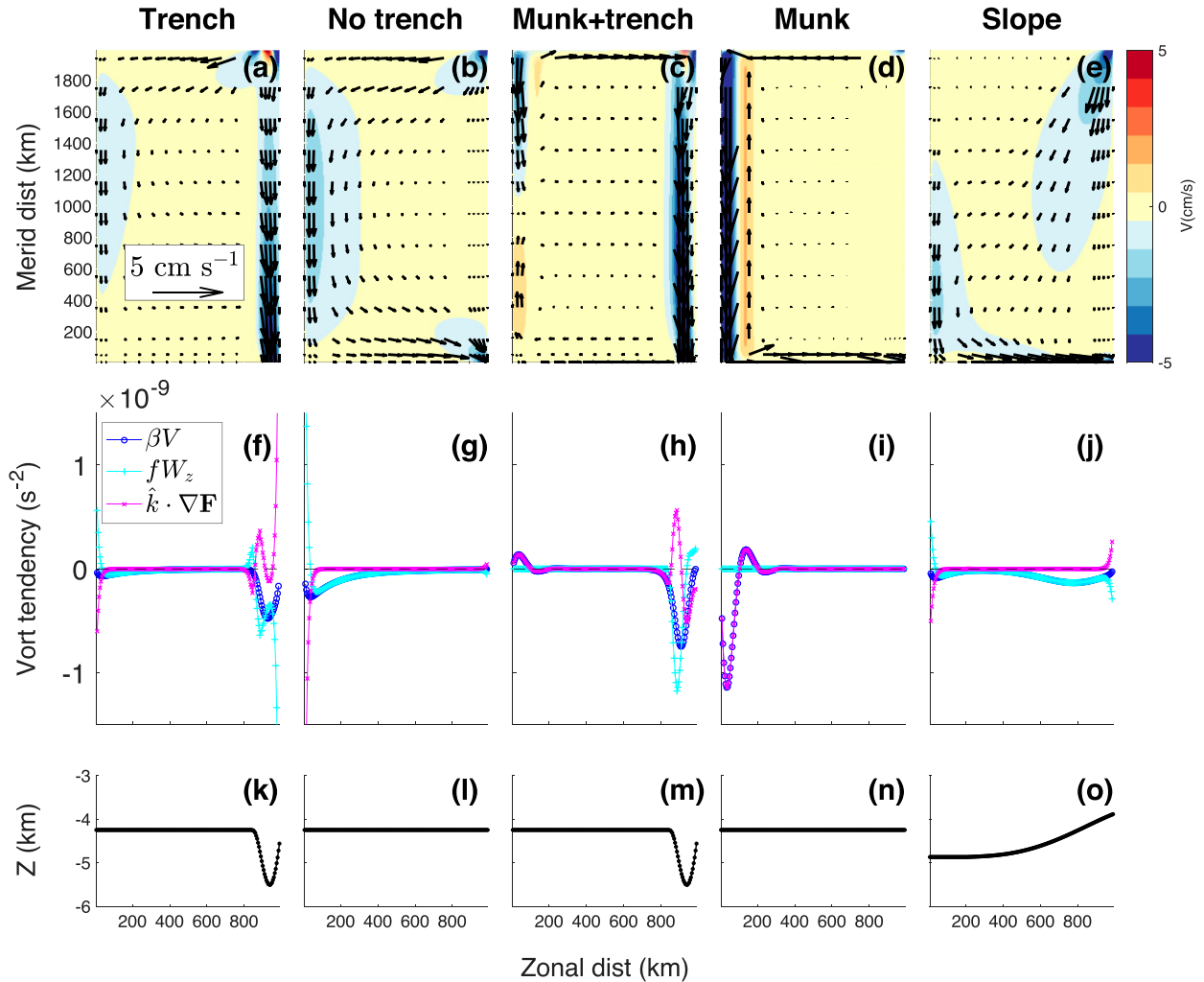


FIG. 6. Results of the vertically integrated simple vorticity model. (a) Northward velocity (colors), and velocity vectors (black arrows) of the full-parameter model [Eq. (12)] forced by a Pacific-like trench. (f) Vorticity budget of the “trench” experiment. (k) The bathymetry profile of the trench experiment. (b),(g),(l) As in (a), (f), and (k), but for the full-parameter model forced by a flat bottom. (c),(h),(m) As in (a), (f), and (k), but for the no-stratification model forced by a trench. (d),(i),(n) As in (a), (f), and (k), but for the no-stratification Munk-like model forced by a flat bottom. (e),(j),(o) As in (a), (f), and (k), but for the full-parameter model forced by a broad Atlantic-like slope.

We ran idealized GCM configurations with simplified bathymetry, specified inflow/outflow boundary conditions, no wind forcing, horizontally uniform temperature surface forcing, and parameterized eddy effects. These runs successfully simulate DEBCs in the three idealized ocean basin configurations corresponding to the southeast Pacific, Atlantic and Indian DEBCs. This implies that the wind forcing and gradients in surface buoyancy forcing are not essential parts in the local DEBC dynamics. Of course, wind and buoyancy forcings, possibly at high latitudes, are likely to play a part in driving the inflows and outflows forcing the DEBCs. The vorticity budget of the DEBCs reveals two dynamical regions in the cross-stream direction. In the outer and wider region, the advection of planetary vorticity by the southward flow is balanced by vortex stretching ( $\beta v \approx f w_z$ ) induced by bottom topography

and parameterized eddy temperature mixing. This vorticity balance is typical of the ocean interior rather than boundary currents, although the topographic stretching effect has been found to be important for western boundary currents as well (Yeager and Jochum 2009).

There is, however, a narrow inner boundary layer near the eastern boundary and away from the core of the DEBC, where horizontal friction balances horizontal diffusion in the vorticity budget. Such a boundary layer has been proposed and studied before in linear stratified theories (Barcilon and Pedlosky 1967). Further studies identified two boundary layers near lateral eastern boundaries, where the thicker one is characterized by a balance between the  $\beta$  term and diffusion (LaCasce 2004; Gjermundsen and LaCasce 2017), or between horizontal and vertical diffusion on an  $f$  plane (Pedlosky 1974);

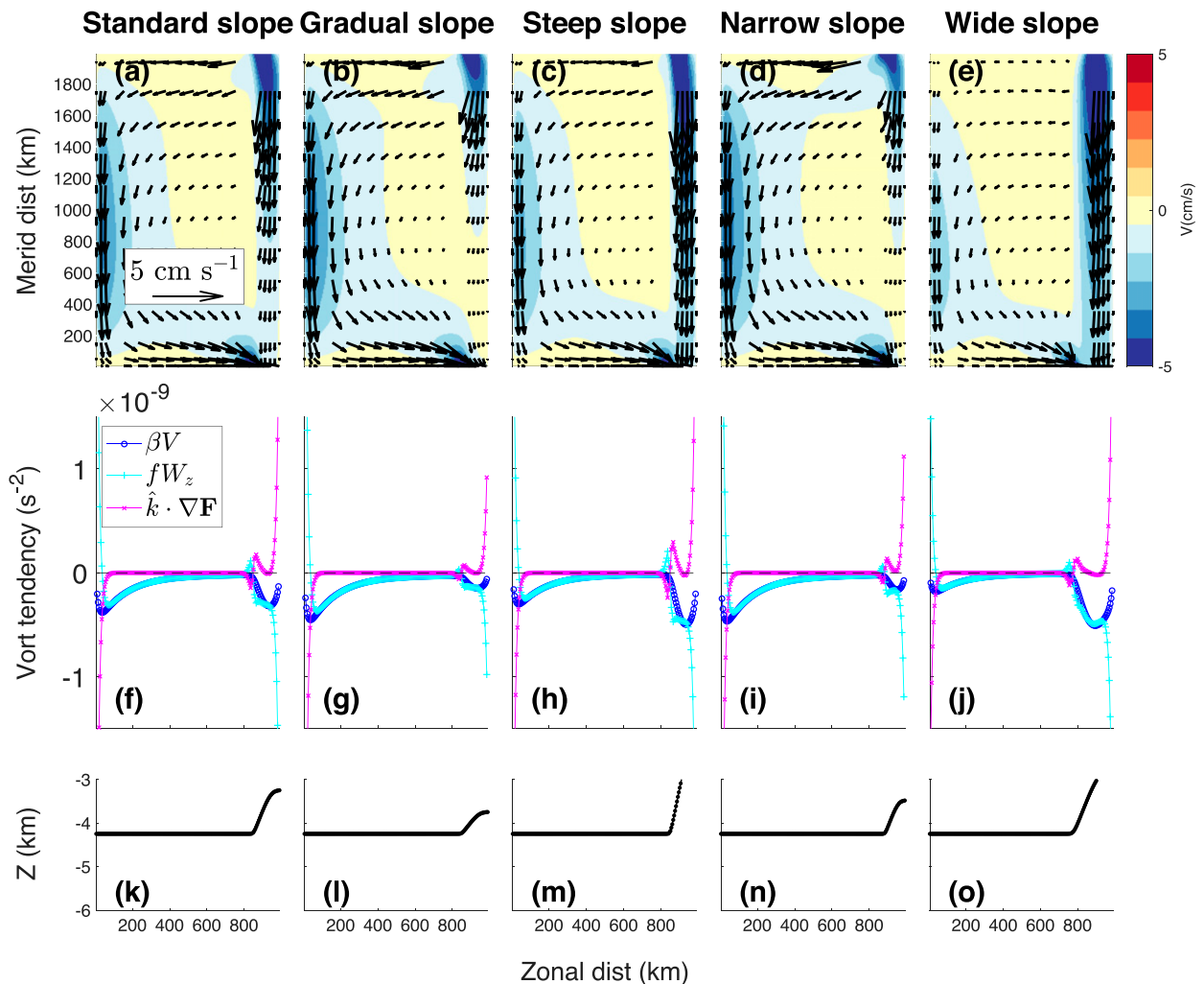


FIG. 7. The sensitivity of the simple vorticity model solution to bathymetry. (a) Northward velocity (colors), and velocity vectors (black arrows) of the full-parameter model “standard slope” case. (f) Three-term vorticity budget of the standard slope experiment. (k) The bathymetry profile of the standard slope experiment. (b),(g),(l) As in (a), (f), and (k), but for the “gradual slope” case. (c),(h),(m) As in (a), (f), and (k), but for the “steep slope” case. (d),(i),(n) As in (a), (f), and (k), but for the “narrow slope” case. (e),(j),(o) As in (a), (f), and (k), but for the “wide slope” case.

the inner one is characterized by a similar balance to that in [Barcilon and Pedlosky \(1967\)](#). These eastern boundary solutions can be determined by a global constraint of no net upwelling, instead of by local dynamics ([LaCasce 2004](#); [Gjermundsen and LaCasce 2017](#)). Alternatively, eastern boundary stratification, which must be prescribed in classical thermocline theories ([Luyten et al. 1983](#); [Rhines and Young 1982](#)), can be calculated by a global constraint balancing surface transformation of water masses with interior transformation by vertical mixing ([Tziperman 1986](#); [Miller et al. 2020](#)). A similar boundary layer decomposition is also found in the vorticity budget of near-surface eastern boundary currents driven by a surface meridional buoyancy gradient ([Bire and Wolfe 2018](#)).

The simple linear vorticity model derived here, based on the semigeostrophic approximation ([McCreary et al. 1986](#);

[Bire and Wolfe 2018](#)), was used to further study the DEBC dynamics. The model is fourth order in longitude and therefore has four eigensolutions. Two of these solutions decay from the western boundary and two from the eastern boundary. This differs from the [Munk \(1950\)](#) WBC model, where there are two comparable western decaying scales, one eastern decaying solution and one constant solution. Because there is only one eastern boundary decaying solution, the Munk model cannot satisfy the no normal flow boundary condition on the eastern boundary and it needs to be satisfied by the interior solution ([Munk 1950](#)). One of the eastern decaying solutions found here has a very large decay scale, comparable to the basin scale, thus, as in the Munk model, the eastern boundary can only support a boundary condition on the parallel flow, via the sublayer showing a balance of horizontal diffusion and friction.

To further investigate the role of topography, we integrated the simple vorticity model vertically from the ocean bottom, where vertical velocity is induced by bathymetry, to above the DEBC core. This model then successfully reproduced the results and the vorticity balances observed in the idealized GCM simulations. We find that the vertical stretching that drives the DEBCs over much of their width is affected by flows crossing bottom topography and by horizontal parameterized eddy temperature mixing within the water column. This is consistent with the idealized GCM experiments indicating that DEBCs would not have existed without the stretching-inducing bathymetry near the eastern boundary, whether a trench as in the Pacific or a slope as in the Atlantic and Indian Oceans.

This paper extends the work of Yang et al. (2020b) which only discussed the Pacific DEBC, and the realistic regional simulations of the southeast Atlantic/Indian/Pacific of Yang et al. (2020a). We consider here idealized geometric configurations corresponding to the three Southern Hemisphere DEBC sites and obtain several additional insights:

- (i) The simple vorticity model is used to show that topography and eddy mixing comparably force the vortex stretching driving the DEBC.
- (ii) We explore the sensitivity to model parameters and find that the two eastern-boundary decay scales can become similar for high vertical diffusivity, making the DEBC more of an actual boundary current (Figs. S3–S6 and Tziperman 1987; Kawase 1987).
- (iii) Using the idealized GCM configurations, we find that the DEBC strength and latitudinal extent depend on the slope width.

We note that the DEBC in our idealized Atlantic-like configuration is bottom intensified, unlike the middepth maximum it shows in SOSE and the realistic simulations (Yang et al. 2020a). This may be a result of the lack of eddies in this idealized configuration, and in a follow-up work we find that adding eddies to this configuration leads to eddy thickness transport, which produces a correct South Atlantic DEBC vertical structure (Yang and Tziperman 2021, manuscript submitted to *Ocean Modell.*). In another follow-up work, we will use global idealized configurations to study the relationship between the DEBCs and the large-scale circulation, rather than prescribing inflows and outflows as done here.

There are several caveats that should be mentioned. First, only the local dynamics of the DEBCs were addressed using the regional configurations used here, leaving open the question of what drives the inflow and outflow boundary conditions that are prescribed here. In the idealized Pacific Ocean configuration, the prescribed inflow from the northern boundary flows along the northern and western sponge layers, and then proceeds eastward to feed the DEBC. A more appropriate boundary condition would therefore have been a prescription of a slow input from the western boundary, which would have also been consistent with the driving of the DEBC in SOSE (Yang et al. 2020a). The configuration used here therefore cannot be used to study how the flow that feeds the DEBCs is embedded in the large-scale circulation, but the lessons regarding the local DEBC dynamics should be robust. Second,

although the wind forcing and surface buoyancy forcing are not found to be important for the local dynamics of the DEBCs, such forcing, especially at higher latitudes, is very likely important driving mechanisms for the circulation that leads to the imposed inflow/outflow boundary conditions. The lack of such surface forcing also leads to the absence of explicit eddies in our simulation, which were found to be important in the companion work (Yang et al. 2020a) especially in the Indian and Atlantic basins. The simple vorticity model used here is derived heuristically, is based on crude assumptions such as a Gaussian vertical structure although the problem is not separable in the horizontal and vertical dimensions, and does not represent a rigorous formal solution to the linearized dynamics. Furthermore, this simple model does not resolve eddies explicitly, although they have been found to be important in the local dynamics of the DEBCs in the GCM simulations. Although it does not address the larger basin-scale dynamics, this simple vorticity model still provides significant insights into the local vorticity dynamics of DEBCs.

*Acknowledgments.* We thank the reviewers for their knowledgeable and helpful comments. XY and ET are supported by the National Science Foundation physical oceanography program, Grant OCE-1535800. KS is supported by NSF OCE-1536045. We would like to acknowledge high-performance computing support from Cheyenne provided by NCAR's Computational and Information Systems Laboratory, sponsored by the National Science Foundation. ET thanks the Weizmann Institute for its hospitality during parts of this work.

The MITgcm 3D ocean model used for this work is a community-developed model available for download from [http://mitgcm.org/public/source\\_code.html](http://mitgcm.org/public/source_code.html). All data, MITgcm modifications, vorticity model codes, and analysis scripts used in this work, are archived in the “Open Science Framework,” which is a public, community-supported repository, at <https://osf.io/agtmq/>. These codes are publicly available, with no restrictions. The authors declare no conflict of interests.

## REFERENCES

- Barcilon, V., and J. Pedlosky, 1967: A unified linear theory of homogeneous and stratified rotating fluids. *J. Fluid Mech.*, **29**, 609–621, <https://doi.org/10.1017/S0022112067001053>.
- Benthuyens, J., R. Furue, J. P. McCreary, N. L. Bindoff, and H. E. Phillips, 2014: Dynamics of the Leeuwin Current: Part II. Impacts of mixing, friction, and advection on a buoyancy-driven eastern boundary current over a shelf. *Dyn. Atmos. Oceans*, **65**, 39–63, <https://doi.org/10.1016/j.dynatmoce.2013.10.004>.
- Bire, S., 2019: Eddy dynamics of eastern boundary currents. Ph.D. thesis, Stony Brook University, 132 pp.
- , and C. L. Wolfe, 2018: The role of eddies in buoyancy-driven eastern boundary currents. *J. Phys. Oceanogr.*, **48**, 2829–2850, <https://doi.org/10.1175/JPO-D-18-0040.1>.
- Capet, X. J., P. Marchesiello, and J. McWilliams, 2004: Upwelling response to coastal wind profiles. *Geophys. Res. Lett.*, **31**, L13311, <https://doi.org/10.1029/2004GL020123>.
- Choboter, P., R. Samelson, and J. Allen, 2005: A new solution of a nonlinear model of upwelling. *J. Phys. Oceanogr.*, **35**, 532–544, <https://doi.org/10.1175/JPO2697.1>.
- Furue, R., J. P. McCreary, J. Benthuyens, H. E. Phillips, and N. L. Bindoff, 2013: Dynamics of the Leeuwin Current: Part I.

- Coastal flows in an inviscid, variable-density, layer model. *Dyn. Atmos. Oceans*, **63**, 24–59, <https://doi.org/10.1016/j.dynatmoce.2013.03.003>.
- Gent, P. R., and J. C. McWilliams, 1990: Isopycnal mixing in ocean circulation models. *J. Phys. Oceanogr.*, **20**, 150–155, [https://doi.org/10.1175/1520-0485\(1990\)020<0150:IMIOCM>2.0.CO;2](https://doi.org/10.1175/1520-0485(1990)020<0150:IMIOCM>2.0.CO;2).
- Gjermundsen, A., and J. H. LaCasce, 2017: Comparing the linear and nonlinear buoyancy-driven circulation. *Tellus*, **69A**, 1299282, <https://doi.org/10.1080/16000870.2017.1299282>.
- Hickey, B. M., 1979: The California Current system—Hypotheses and facts. *Prog. Oceanogr.*, **8**, 191–279, [https://doi.org/10.1016/0079-6611\(79\)90002-8](https://doi.org/10.1016/0079-6611(79)90002-8).
- Hogg, N. G., and A. M. Thurnherr, 2005: A zonal pathway for NADW in the South Atlantic. *J. Oceanogr.*, **61**, 493–507, <https://doi.org/10.1007/s10872-005-0058-7>.
- Holloway, G., 1992: Representing topographic stress for large-scale ocean models. *J. Phys. Oceanogr.*, **22**, 1033–1046, [https://doi.org/10.1175/1520-0485\(1992\)022<1033:RTSFLS>2.0.CO;2](https://doi.org/10.1175/1520-0485(1992)022<1033:RTSFLS>2.0.CO;2).
- Hughes, C. W., and B. A. De Cuevas, 2001: Why western boundary currents in realistic oceans are inviscid: A link between form stress and bottom pressure torques. *J. Phys. Oceanogr.*, **31**, 2871–2885, [https://doi.org/10.1175/1520-0485\(2001\)031<2871:WWBCIR>2.0.CO;2](https://doi.org/10.1175/1520-0485(2001)031<2871:WWBCIR>2.0.CO;2).
- Kawase, M., 1987: Establishment of deep ocean circulation driven by deep-water production. *J. Phys. Oceanogr.*, **17**, 2294–2317, [https://doi.org/10.1175/1520-0485\(1987\)017<2294:EODOCD>2.0.CO;2](https://doi.org/10.1175/1520-0485(1987)017<2294:EODOCD>2.0.CO;2).
- LaCasce, J., 2004: Diffusivity and viscosity dependence in the linear thermocline. *J. Mar. Res.*, **62**, 743–769, <https://doi.org/10.1357/0022240042880864>.
- Luyten, J. R., J. Pedlosky, and H. Stommel, 1983: The ventilated thermocline. *J. Phys. Oceanogr.*, **13**, 292–309, [https://doi.org/10.1175/1520-0485\(1983\)013<0292:TVT>2.0.CO;2](https://doi.org/10.1175/1520-0485(1983)013<0292:TVT>2.0.CO;2).
- Marshall, J., A. Adcroft, C. Hill, L. Perelman, and C. Heisey, 1997: A finite-volume, incompressible Navier Stokes model for studies of the ocean on parallel computers. *J. Geophys. Res.*, **102**, 5753–5766, <https://doi.org/10.1029/96JC02775>.
- Mazloff, M. R., P. Heimbach, and C. Wunsch, 2010: An eddy-permitting Southern Ocean state estimate. *J. Phys. Oceanogr.*, **40**, 880–899, <https://doi.org/10.1175/2009JPO4236.1>.
- McCreary, J. P., 1981: A linear stratified ocean model of the equatorial undercurrent. *Philos. Trans. Roy. Soc. London*, **298A**, 603–635, <https://doi.org/10.1098/rsta.1981.0002>.
- , and S.-Y. Chao, 1985: Three-dimensional shelf circulation along an eastern ocean boundary. *J. Mar. Res.*, **43**, 13–36, <https://doi.org/10.1357/002224085788437316>.
- , S. R. Shetye, and P. K. Kundu, 1986: Thermohaline forcing of eastern boundary currents: With application to the circulation off the west coast of Australia. *J. Mar. Res.*, **44**, 71–92, <https://doi.org/10.1357/002224086788460184>.
- , P. K. Kundu, and S.-Y. Chao, 1987: On the dynamics of the California current system. *J. Mar. Res.*, **45**, 1–32, <https://doi.org/10.1357/002224087788400945>.
- , Y. Fukamachi, and P. Lu, 1992: A nonlinear mechanism for maintaining coastally trapped eastern boundary currents. *J. Geophys. Res.*, **97**, 5677–5692, <https://doi.org/10.1029/92JC00035>.
- Miller, M., X. Yang, and E. Tziperman, 2020: Reconciling the observed mid-depth exponential ocean stratification with weak interior mixing and Southern Ocean dynamics via boundary-intensified mixing. *Eur. Phys. J. Plus*, **135**, 375, <https://doi.org/10.1140/epjp/s13360-020-00375-y>.
- Munk, W. H., 1950: On the wind-driven ocean circulation. *J. Meteor.*, **7**, 80–93, [https://doi.org/10.1175/1520-0469\(1950\)007<0080:OTWDOC>2.0.CO;2](https://doi.org/10.1175/1520-0469(1950)007<0080:OTWDOC>2.0.CO;2).
- Nof, D., and D. B. Olson, 1993: How do western abyssal currents cross the equator? *Deep-Sea Res. I*, **40**, 235–255, [https://doi.org/10.1016/0967-0637\(93\)90002-K](https://doi.org/10.1016/0967-0637(93)90002-K).
- Park, Y.-G., 2006: Dependence of an eastern boundary current on the horizontal resolution in thermally driven circulations. *J. Geophys. Res.*, **111**, C09005, <https://doi.org/10.1029/2005JC003362>.
- Pedlosky, J., 1974: Longshore Currents, upwelling and bottom topography. *J. Phys. Oceanogr.*, **4**, 214–226, [https://doi.org/10.1175/1520-0485\(1974\)004<0214:LCUABT>2.0.CO;2](https://doi.org/10.1175/1520-0485(1974)004<0214:LCUABT>2.0.CO;2).
- , 1987: *Geophysical Fluid Dynamics*. 2nd ed. Springer-Verlag, 710 pp.
- , 2003: Thermally driven circulations in small oceanic basins. *J. Phys. Oceanogr.*, **33**, 2333–2340, [https://doi.org/10.1175/1520-0485\(2003\)033<2333:TDCISO>2.0.CO;2](https://doi.org/10.1175/1520-0485(2003)033<2333:TDCISO>2.0.CO;2).
- Peliz, Á., J. Dubert, D. B. Haidvogel, and B. Le Cann, 2003: Generation and unstable evolution of a density-driven eastern Poleward Current: The Iberian Poleward Current. *J. Geophys. Res.*, **108**, 3268, <https://doi.org/10.1029/2002JC001443>.
- Rhines, P. B., and W. R. Young, 1982: A theory of the wind-driven circulation. I. Mid-ocean gyres. *J. Mar. Res.*, **40**, 559–596.
- Samelson, R., 2017: Time-dependent linear theory for the generation of poleward undercurrents on eastern boundaries. *J. Phys. Oceanogr.*, **47**, 3037–3059, <https://doi.org/10.1175/JPO-D-17-0077.1>.
- Sloyan, B. M., and S. R. Rintoul, 2001: The Southern Ocean limb of the global deep overturning circulation. *J. Phys. Oceanogr.*, **31**, 143–173, [https://doi.org/10.1175/1520-0485\(2001\)031<0143:TSOLOT>2.0.CO;2](https://doi.org/10.1175/1520-0485(2001)031<0143:TSOLOT>2.0.CO;2).
- Stephens, J. C., and D. P. Marshall, 2000: Dynamical pathways of Antarctic Bottom Water in the Atlantic. *J. Phys. Oceanogr.*, **30**, 622–640, [https://doi.org/10.1175/1520-0485\(2000\)030<0622:DPOABW>2.0.CO;2](https://doi.org/10.1175/1520-0485(2000)030<0622:DPOABW>2.0.CO;2).
- Thompson, R. O., 1984: Observations of the Leeuwin Current off Western Australia. *J. Phys. Oceanogr.*, **14**, 623–628, [https://doi.org/10.1175/1520-0485\(1984\)014<0623:OOTLCO>2.0.CO;2](https://doi.org/10.1175/1520-0485(1984)014<0623:OOTLCO>2.0.CO;2).
- Toole, J. M., and B. A. Warren, 1993: A hydrographic section across the subtropical South Indian Ocean. *Deep-Sea Res. I*, **40**, 1973–2019, [https://doi.org/10.1016/0967-0637\(93\)90042-2](https://doi.org/10.1016/0967-0637(93)90042-2).
- Tziperman, E., 1986: On the role of interior mixing and air–sea fluxes in determining the stratification and circulation of the oceans. *J. Phys. Oceanogr.*, **16**, 680–693, [https://doi.org/10.1175/1520-0485\(1984\)014<0623:OOTLCO>2.0.CO;2](https://doi.org/10.1175/1520-0485(1984)014<0623:OOTLCO>2.0.CO;2).
- , 1987: The Mediterranean outflow as an example of a deep buoyancy-driven flow. *J. Geophys. Res.*, **92**, 14 510–14 520, <https://doi.org/10.1029/JC092iC13p14510>.
- van Sebille, E., W. E. Johns, and L. M. Beal, 2012: Does the vorticity flux from Agulhas rings control the zonal pathway of NADW across the South Atlantic? *J. Geophys. Res.*, **117**, C05037, <https://doi.org/10.1029/2011JC007684>.
- Weaver, A. J., and J. H. Middleton, 1989: On the dynamics of the Leeuwin Current. *J. Phys. Oceanogr.*, **19**, 626–648, [https://doi.org/10.1175/1520-0485\(1989\)019<0626:OTDOTL>2.0.CO;2](https://doi.org/10.1175/1520-0485(1989)019<0626:OTDOTL>2.0.CO;2).
- Well, R., W. Roether, and D. P. Stevens, 2003: An additional deep-water mass in Drake Passage as revealed by <sup>3</sup>He data. *Deep-Sea Res. I*, **50**, 1079–1098, [https://doi.org/10.1016/S0967-0637\(03\)00050-5](https://doi.org/10.1016/S0967-0637(03)00050-5).
- Wolfe, C., and S. Bire, 2019: Eastern boundary currents an overturning in buoyancy-driven basins. *22nd Conf. on Atmospheric*

- and *Oceanic Fluid Dynamics*, Portland, ME, Amer. Meteor. Soc., 8.5, <https://ams.confex.com/ams/22FLUID/meetingapp.cgi/Paper/360227>.
- Wolfe, C. L., and P. Cessi, 2009: Overturning circulation in an eddy-resolving model: The effect of the pole-to-pole temperature gradient. *J. Phys. Oceanogr.*, **39**, 125–142, <https://doi.org/10.1175/2008JPO3991.1>.
- Yang, X., E. Tziperman, and K. Speer, 2020a: Deep eastern boundary currents: Realistic simulations and vorticity budgets. *J. Phys. Oceanogr.*, **50**, 3077–3094, <https://doi.org/10.1175/JPO-D-20-0002.1>.
- , —, and —, 2020b: Dynamics of deep eastern boundary currents. *Geophys. Res. Lett.*, **47**, e2019GL085396, <https://doi.org/10.1029/2019GL085396>.
- Yeager, S. G., and M. Jochum, 2009: The connection between Labrador Sea buoyancy loss, deep western boundary current strength, and Gulf Stream path in an ocean circulation model. *Ocean Modell.*, **30**, 207–224, <https://doi.org/10.1016/j.oceomod.2009.06.014>.